Effect of Laser-Matter Interaction on Molten Pool Flow and Keyhole Dynamics

Nadia Kouraytem,[1] Xuxiao Li,[1] Ross Cunningham,[2] Cang Zhao,[3] Niranjan Parab,[3] Tao Sun,[3] Anthony D. Rollett,[2] Ashley D. Spear,[1] and Wenda Tan[1,*]

[1] *Department of Mechanical Engineering, The University of Utah, Salt Lake City, Utah 84112, USA*

[2] *Department of Materials Science and Engineering, Carnegie Mellon University, Pittsburgh, Pennsylvania 15213, USA*

[3] *X-ray Science Division, Advanced Photon Source, Argonne National Laboratory, Lemont, Ilinois 60439, USA*

(Received 31 March 2019; published XX XX 2019)

Laser-induced keyholing occurs in additive manufacturing and welding processes, but the keyhole dynamics have not been well understood. A multiphase and multiphysics numerical model is used to predict the keyhole shapes recorded in the experimental observations and to predict transient and nonuniform distributions of laser absorption, temperature, and flow velocity in the process. When compared against data from a state-of-the-art dynamic x-ray radiography technique, good agreement is found for the keyhole shapes and fluctuation of the gas-liquid interface, thereby validating the simulation method. A detailed discussion is then given to elucidate the effects of laser absorption on the dynamic behavior of the front and rear keyhole walls. A quantitative comparison of different driving forces on the keyhole is also given to evaluate their significance to the keyhole dynamics.

DOI: 10.1103/PhysRevApplied.0.XXXXXX

I. INTRODUCTION

The keyholing phenomenon is frequently found in laser-based metal additive manufacturing and welding processes. As shown in Fig. 1, a keyhole starts with a laser of an adequately high power intensity that induces not only melting but also surface evaporation of the metals. The high-speed flow of evaporated metal (denoted by the purple arrows) exerts a recoil pressure on the molten pool surface, which pushes the molten metal aside to create a keyhole. The gas-liquid interface of the keyhole usually exhibits strong fluctuations, which is found to be the major reason for the formation of spatters and pores [1–4]. The detailed fluctuation dynamics of laser-induced keyholes is complex and not fully understood. Extensive experimental and modeling efforts have focused on investigating this issue.

The experimental investigations of keyhole dynamics are primarily carried out through visualization of the keyhole shape. Optical imaging has been used most frequently to observe the keyhole dynamics from the top view [3,5–8] and side view [9–11]. Alternatively, x-ray imaging provides a unique capability to penetrate nondestructively opaque metals for *in situ* observation of keyhole dynamics without disturbing the process [1,2,4,12–17]. These visualization-based works have collectively disclosed that the keyhole adopts different shapes as a function of power and speed and its internal surface generally fluctuates noticeably. The shape and fluctuation magnitude and frequency are affected by a variety of factors, including laser parameters (laser power, scanning speed, pulse width, duty cycle, etc.); the protective gas environment; and properties of substrate metals.

Since the absorbed laser light is the dominant energy source that induces keyhole formation, it is critical to measure the laser absorption by the keyhole. The measurements using calorimetry [18,19] or the integrated sphere method [20] have clearly revealed that the total laser absorption is noticeably increased when a keyhole is formed and that the increment in absorptivity is highly dependent on the keyhole geometry. This originates in the multiple-reflection phenomenon of the laser light inside the keyhole. The integrated sphere method can also capture the dynamic fluctuation of laser absorption [20], which is attributed to the dynamic fluctuation of keyhole geometry.

Despite the significant advancements in experimental observation of keyhole dynamics, important information regarding keyhole dynamics is still missing. First, the current techniques cannot measure the spatial distribution of the laser absorption on the keyhole wall, which is expected to be nonuniform and has decisive effects on the keyhole dynamics. Furthermore, the keyhole evolution is closely coupled with the metal evaporation and thermofluidic flows of the liquid/vapor metals, both of which are difficult to measure through experimentation, especially when the metals are in a high-temperature and dynamic

*wenda.tan@mech.utah.edu

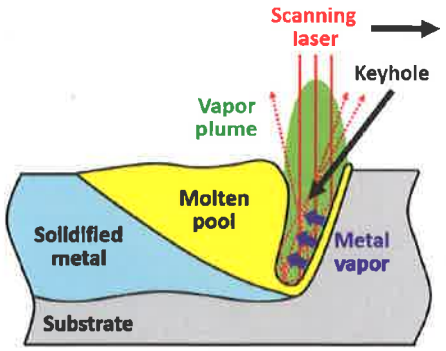

Q4 F1:1 FIG. 1. Schematic of laser-induced keyhole.

state. Without the above information, it is infeasible to obtain a complete understanding of the keyhole dynamics.

Numerical modeling complements experiments and enhances the understanding of keyhole dynamics by providing information that is difficult to measure with experiments. Ray-tracing models are widely used to simulate the multiple reflections and partial absorption of laser light inside the keyhole. The models can successfully predict the nonuniform laser absorption in ~~the~~ keyhole of different shapes [21–26] and have well demonstrated that the laser absorption is highly dependent on the keyhole shape. In the more recent multiphysics modeling of keyhole dynamics [27–39], the ray-tracing model is coupled with a computational thermofluidic dynamics model and a free surface tracking model (based on level-set, volume-of-fluid, or arbitrary Lagrangian-Eulerian methods). The ray-tracing model can predict the distribution of laser absorption intensity on the keyhole wall, which is used in the thermofluidic model to drive the variations of temperature field and fluid flow in both the molten pool and surrounding gaseous region. The predicted flow velocity will inform the surface tracking model, which updates the location of the metal surface, a part of which is the keyhole wall. While these multiphysics models have already been used to investigate various issues regarding the formation and dynamic evolution of laser-induced keyholes, their predictions of the keyhole shape and fluctuation have rarely been validated against physical measurements of real keyholes. Hence, the quantitative accuracy of the simulations is still not clear.

In this paper, we present a combination of the state-of-the-art dynamic x-ray radiography (DXR) experimental measurements with an in-house multiphysics numerical model to investigate the dynamic phenomena of laser-induced keyholes in stainless steel (SS) 304. The DXR system at the Advanced Photon Source (APS) is first used to perform *in situ* observation of the keyhole dynamics for a wide range of laser powers and scanning speeds. The multiphysics model is then used to simulate the three-dimensional (3D) dynamic keyhole phenomenon. The model can well replicate the keyhole shape and fluctuation observed in the DXR experiments. The simulation results are further leveraged to understand the effects of nonuniform laser absorption on temperature and flow fields of the liquid/vapor metals as well as the dynamic keyhole behavior.

II. RESULTS

A. Dynamic x-ray radiography experiments

In our DXR experiments, a high-energy, high-flux x-ray beam penetrates through the opaque metal substrate to image the keyhole shape with high spatial and temporal resolutions (see Appendix A for the details). The typical keyhole shapes generated by different laser powers and scanning speeds are shown in Fig. 2. To quantify the keyhole shape, we schematically define the local keyhole depth d_k, local keyhole width w_k, and local front keyhole wall inclination α in the inset of Fig. 2. Here, we define the

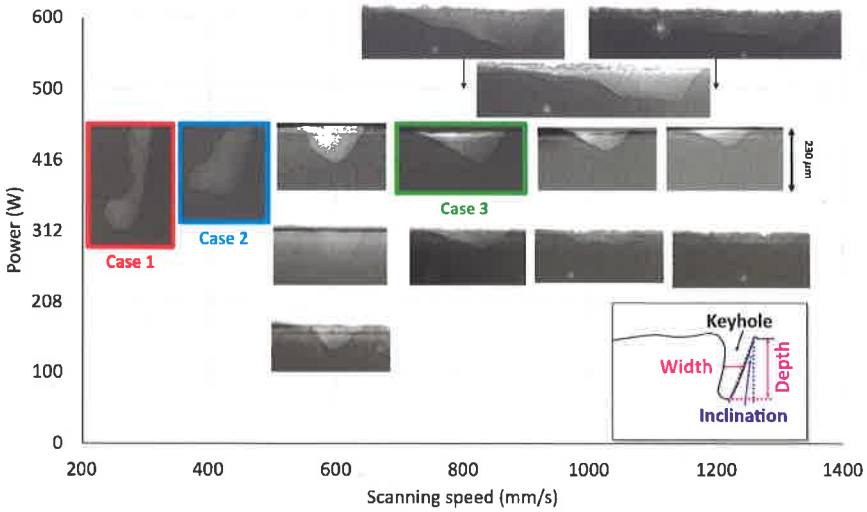

FIG. 2. Keyhole processing map for SS304 with different laser powers and scanning speeds. The colored boxes highlight the three selected cases of typical keyhole shapes for further investigation. For all three cases, the experiments are performed at the same laser power $P =$ 416 W and varying scanning speeds: case 1 at $V = 300$ mm/s; case 2 at $V =$ 400 mm/s; case at 3 $V = 800$ mm/s. The inset sketch defines the geometrical parameters used in the course of the study.

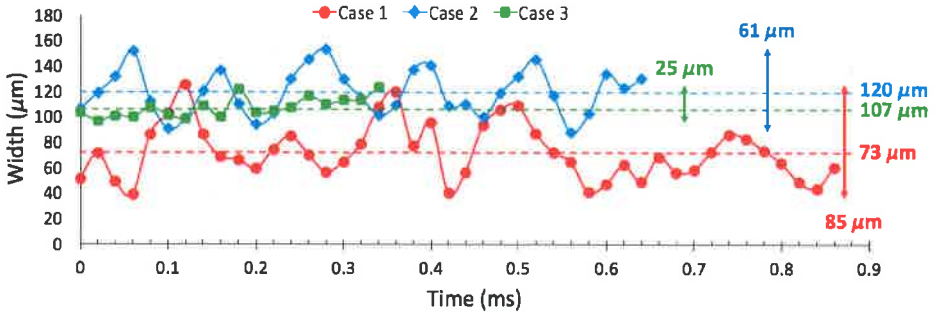

F3:1 FIG. 3. Temporal variation of keyhole width in the three selected cases: case 1 at $P = 416$ W, $V = 300$ mm/s; case 2 at $P = 416$ W,
F3:2 $V = 400$ mm/s; case 3 at $P = 416$ W, $V = 800$ mm/s. The solid dotted lines show the instantaneous width, the dashed lines show the
F3:3 average width, and the double-headed arrows show the magnitudes of width fluctuation.

keyhole width as the horizontal distance between the front and rear keyhole wall at mid-depth.

The effects of laser scanning speed are investigated as a series of experiments at constant laser power $P = 416$ W. With increasing laser scanning speed ($V = 300 - 1200$ mm/s), the keyhole depth decreases from around 370 μm to around 118 μm, and the front wall inclination α increases from around 9° to 47°. These trends are consistent with those reported in Ref. [5]. The keyhole width varies along the depth direction in all cases. When the laser scanning speed is ≤ 400 mm/s, the keyhole is generally wider at the lower portion than on the upper portion. As the scanning speed is increased to be ≥ 600 mm/s, the upper portion of the keyhole becomes wider than the lower portion. Three typical cases are selected from this series (case 1 in the red box, case 2 in the blue box, and case 3 in the green box in Fig. 2) for direct comparison with numerical simulation. In case 1, with the combination of high laser power of $P = 416$ W and low scanning speed of $V = 300$ mm/s, the keyhole presents the traditional deep and slender shape. As the scanning speed increases in case 2 to $V = 400$ mm/s, the keyhole becomes shallower and wider, presenting a quasiquadrilateral shape. A further increase of the scanning speed to $V = 800$ mm/s in the green case 3 changes the keyhole to a triangular shape.

Varying the laser power is investigated at a constant scanning speed of $V = 600$ mm/s. As the laser power increases from 208 to 416 W, the keyhole depth increases from about 55 to 129 μm, the front wall inclination decreases from around 45° to 34°, the keyhole width at half depth increases from around 68 to 155 μm, and similarly the keyhole width at the top surface increases from about 102 to 220 μm.

While the front keyhole wall is generally stable, which leads to a relatively constant keyhole depth and front-wall inclination, the rear keyhole wall continuously changes its shape and relative location with respect to the front wall. Since the keyhole width is not uniform along the keyhole depth direction, we quantify the general keyhole width with its value at half of the keyhole depth and plot, in Fig. 3, the temporal variation of the keyhole width for the three typical cases. The average keyhole width is the minimum for case 1 of $P = 416$ W and $V = 300$ mm/s (73 μm), indicating that the keyhole is rather narrow when the laser scanning speed is low. With the scanning speed increased to $V = 400$ mm/s and $V = 800$ mm/s, the average keyhole width is noticeably increased in case 2 (120 μm) and case 3 (107 μm).

As the keyhole continuously changes its width around the average value, we quantify the fluctuation of keyhole width by its magnitude and period. The fluctuation magnitude is defined as the difference between the maximum and minimum width in each case and is found to decrease as the laser scanning speed increases from case 1 to case 3 (85, 61, and 25 μm, as delineated by the colored double-headed arrows in Fig. 3). The fluctuation period is defined as the time difference between two adjacent moments when the instantaneous keyhole width decreases from above to below the average value and is found to be around 100 μs in all three cases. This corresponds to a fluctuation frequency of around 10 kHz, which is of the same magnitude as the previous experimental measurements based on acoustic and optical signals [40–42]. Note that the frequency of 10 kHz primarily describes the fluctuation of the entire keyhole. Local fluctuations with higher frequencies are found at different locations and instances on the keyhole wall but the length scale and magnitude of those fluctuations are small and do not significantly affect the overall shape of the keyhole.

B. Multiphysics numerical simulations

Our simulations use a multiphysics model to predict the transient evolution of the 3D keyhole shape and the distributions of temperature, pressure, and flow velocity in the substrate, molten pool, keyhole, and surrounding air. The details of the model are given in Appendix B.

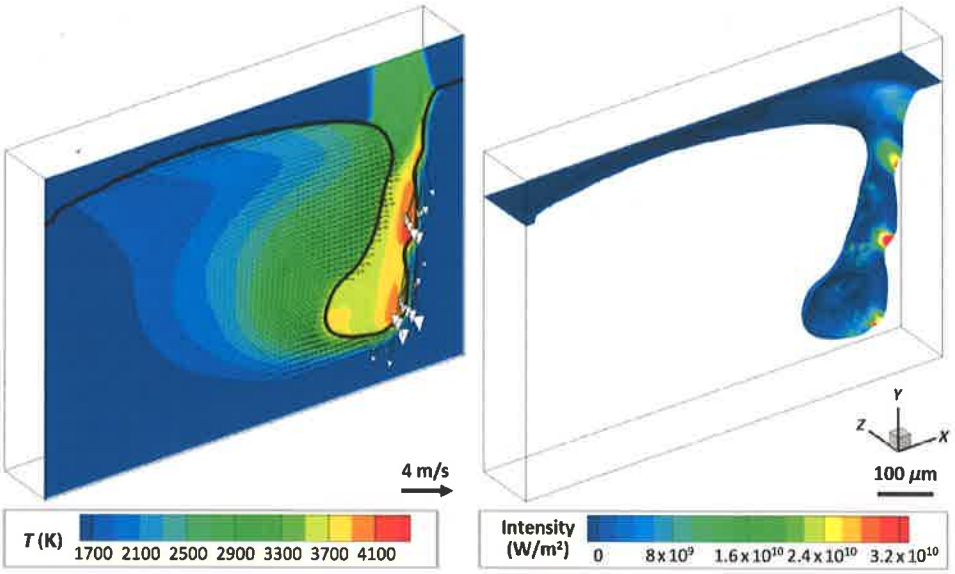

FIG. 4. Typical results of 3D simulation of laser-induced keyhole: (a) predicted temperature and velocity on the 2D center plane (velocity in the gas region is hidden for image clarity); (b) distribution of laser absorption on the 3D keyhole wall. F4:1 F4:2 F4:3 F4:4 F4:5 F4:6 F4:7 F4:8 F4:9

Figure 4 gives an example of typical simulation results, with panel (a) showing the predicted temperature and velocity distributions on the center plane of the track and panel (b) showing the distribution of laser absorption on the 3D keyhole wall.

The three representative cases shown in red (case 1), blue (case 2), and green (case 3) in Fig. 2 are simulated with our multiphysics model. The typical predicted keyhole shapes for the three cases are shown and compared with the DXR observations in Fig. 5. We compare the average keyhole depth (denoted as $\bar{d}_k$), average keyhole width at mid-depth (denoted as $\bar{w}_k$), and average front wall inclination (denoted as $\bar{\alpha}$) from the DXR images and modeling results for the three cases in Table I, which shows a reasonably good agreement. Here, the average values are calculated based on the measurements of corresponding variables at multiple moments from either DXR or simulation results. Furthermore, the model also successfully captures the dynamic keyhole fluctuation. For example, multiple snapshots from different moments in the simulation of case 1 are shown in Figs. 5(f)–5(h), which closely resemble the different keyhole shapes captured by the DXR in Figs. 5(a)–5(c).

Beyond the capability to predict keyhole shape and fluctuation, the model also predicts the laser absorption by the keyhole, as shown in Figs. 5(f)–5(j). By integrating all the absorbed laser power over the entire keyhole, we find the total laser absorption to be approximately 322, 292, and ~186 W for the three respective cases, as given in Table I. With the incident laser power as 416 W, the total laser absorptivity of the keyhole is 80%, 70%, and 48% for the three cases, respectively. These values are very close to

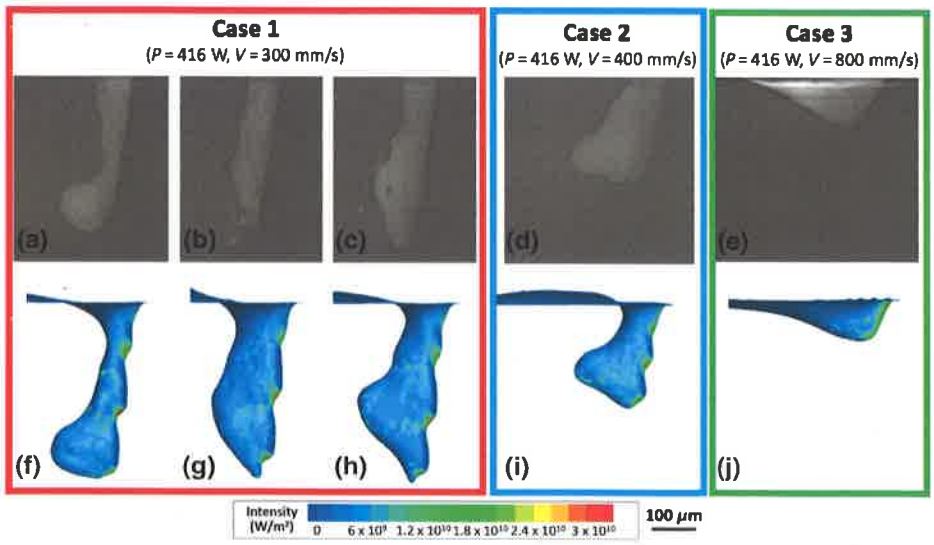

FIG. 5. Comparison of keyhole shapes from DXR observation and simulation results for the three selected cases. (a)–(e) DXR images of the keyhole shapes. (f)–(j) Simulated keyhole shapes and distributions of laser absorption. For illustrative purposes, different instances are shown for case 1, which exhibits the most fluctuation out of the three cases. (a)–(c) Case 1 at times t_0, $t_0 + 140$ ms, and $t_0 + 340$ ms. (f)–(h) Predictions at three selected instances from the simulation. F5:1 F5:2 F5:3 F5:4 F5:5 F5:6 F5:7 F5:8 F5:9 F5:10 F5:11 F5:12 F5:13 F5:14 F5:15

TABLE I. Keyhole dimensions and laser absorption in the three selected cases. The keyhole dimensions are quantified by the keyhole depth, width at mid-depth, and front wall inclination. The laser absorption is quantified by the total absorption, fresh ray absorption, and reflected ray absorption.

		Case 1 $P = 416$ W $V = 300$ mm/s	Case 2 $P = 416$ W $V = 400$ mm/s	Case 3 $P = 416$ W $V = 800$ mm/s
Average depth $\bar{d}_k$ (μm)	DXR	~ 370	~ 250	~ 118
	Model	~ 405	~ 257	~ 103
Average width at mid-depth $\bar{w}_k$ (μm)	DXR	~ 73	~ 120	~ 103
	Model	~ 80	~ 110	~ 140
Average front wall inclination $\bar{\alpha}$ (degrees)	DXR	~ 9	~ 12	~ 37
	Model	~ 9	~ 13	~ 26
Total absorption (W)	Model	332	292	186
Fresh ray absorption (W)	Model	136	135	141
Reflected ray absorption (W)	Model	196	157	45
Reflected ray absorption on front wall (W)	Model	86	70	0
Reflected ray absorption on rear wall (W)	Model	110	87	45

the *in situ* measurement of the laser absorption of a keyhole in SS316 reported in Ref. [19].

III. DISCUSSION

In this section, we leverage the modeling results to discuss the physics of keyhole formation and fluctuation. As explained below, the distribution of laser absorption directly affects the temperature, surface evaporation, and fluid flow in the process, all of which affect the geometry of the front and rear keyhole walls. The keyhole shape, in turn, alters the distribution of laser absorption.

A. Laser absorption in dynamic keyhole

To the best of our knowledge, it is still challenging to measure through experimentation the spatial distribution and temporal variation of laser absorption by a moving keyhole. Our multiphysics model provides quantitative information regarding this issue.

1. Spatial distribution of laser absorption

Figures 6(a)–6(c) show the spatial distribution of laser absorption of all laser rays. We break down the absorption of all laser light into fresh ray absorption and reflected ray absorption. Here, the fresh rays refer to those entering the keyhole directly from the laser source that have not been absorbed by the keyhole wall (as denoted by the solid red lines in Fig. 1). After the fresh rays are partially absorbed by the keyhole wall for the first time, they become reflected rays (as denoted by the dashed red arrows in Fig. 1) and stay inside the keyhole, where they experience multiple additional impingements and partial absorption before they escape from the keyhole. The variations in fresh ray absorption intensity and reflected ray absorption are shown in Figs. 6(d)–6(f) and 6(g)–6(i), respectively. The powers for fresh ray absorption and reflected ray absorption are given in Table I.

The fresh ray absorption takes place solely on the front keyhole wall and the absorption power is very similar in

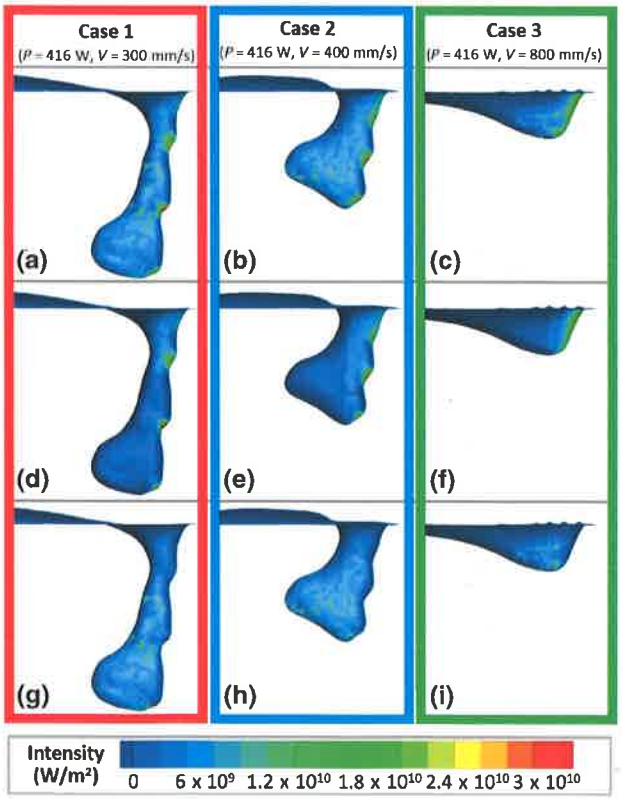

FIG. 6. Distribution of laser absorption intensity: (a)–(c) for all rays, (d)–(f) for fresh rays, and (g)–(h) for reflected rays in the three selected cases.

the three cases (136, 135, and 141 W). With the incident power being 416 W, the average absorptivity for the fresh ray on the front keyhole wall is approximately 33%. The spatial distributions of fresh ray absorption are quite different in the three cases. In cases 1 and 2, noticeable protrusions can be found on the front keyhole wall. The fresh ray absorption is concentrated on the up side of the protrusions and generates very high local absorption intensities ($> 3 \times 10^{10}$ W/m^2). In case 3, the front keyhole wall is flat and the absorption intensity is fairly uniform throughout the front wall (approximately 2.5×10^{10} W/m^2).

The distribution of reflected ray absorption is dependent on the keyhole shape. In case 1, the keyhole has a larger width at the bottom than near the top, so the reflected rays can get trapped in the keyhole to experience multiple (usually more than four) reflections before they escape. The reflected ray absorption is 196 W, much higher than the fresh ray absorption (136 W). The absorption is spread over the entire keyhole in a nonuniform manner, with a slightly larger fraction on the rear wall (110 W) than on the front wall (86 W). The reflected rays can generate absorption intensity as high as 6×10^9 W/m^2 on the keyhole wall. While reflected rays completely determine the keyhole wall temperature on the rear keyhole wall, they just have minor effects on the front wall compared with the high absorption intensities caused by fresh ray absorption on the up side of the protrusion. In case 2, the absorption of reflected rays is distributed in a similar manner as in case 1. In case 3, the keyhole is wide compared to the spot size on top, which offers a large exit for the rays to escape. The reflected rays can be absorbed by the rear keyhole wall at most one time before they leave the keyhole. These rays are not reflected back to the front wall, so there is no reflected ray absorption on the front wall, which lowers the total absorptivity. The decreased total absorptivity in the cases of higher scanning speed and lower molten pool depth is consistent with the experimental observation in Ref. [19].

2. *Temporal variation of laser absorption*

As the keyhole shape changes dynamically during the process, the laser absorption constantly deviates by a small amount from the results shown in Fig. 6 and Table I. Here, we select three scalar variables to quantify the spatial distribution at each moment: total laser absorption, fresh ray absorption, and keyhole wall area above critical absorption intensity (denoted as S_{critical}). The term S_{critical} is the total area of the keyhole wall regions where the local absorption is above the critical power intensity for evaporation, which is estimated to be 1×10^9 W/m^2 [4]. Evaporation is expected to occur in these regions. Figure 7(a) shows larger fluctuations of total laser absorption (approximately 40 W) in cases 1 and 2 than in case 3 (< 10 W). This indicates a less stable keyhole shape in the first two cases, which

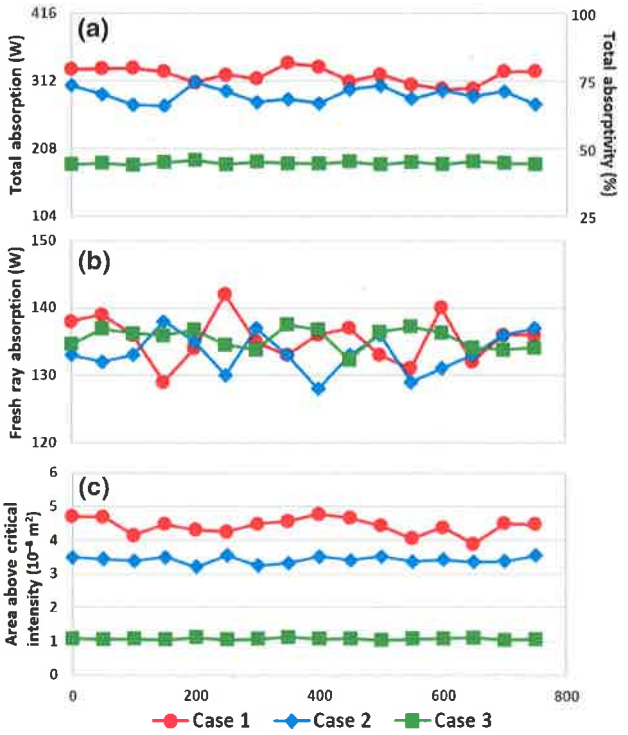

FIG. 7. Temporal variations of (a) total laser absorption and corresponding absorptivity (with respect to the input laser power 416 W), (b) fresh ray absorption, and (c) keyhole wall area with absorption intensity above a critical value. For all three cases, the experiments are performed at the same laser power $P = 416$ W and varying scanning speeds: case 1 at $V = 300$ mm/s; case 2 at $V = 400$ mm/s; case 3 at $V = 800$ mm/s.

is consistent with the experimental observation of keyhole fluctuation in Fig. 3. Figure 7(b) shows very similar fresh ray absorption (between 130 and 140 W) and only minor fluctuations for all three cases. This suggests that fresh ray absorption is not highly dependent on the front wall geometry. This also suggests that the fluctuations of the total absorption in cases 1 and 2 are because of the randomness in the reflected ray absorption. Figure 7(c) shows that the total keyhole wall areas of approximately 4.5×10^{-8} m^2 in case 1 and approximately 3.5×10^{-8} m^2 in case 2 (both with fluctuations of $> 3 \times 10^{-9}$ m^2) have sufficient laser absorption to trigger local evaporation. The regions include the up side of the protrusions on the front keyhole wall and the scattered locations on the rear keyhole wall. In case 3, the laser absorption of around 1×10^{-8} m^2 (with a fluctuation of $< 1 \times 10^{-9}$ m^2) of the keyhole wall can be above the critical intensity. The regions include the entire front keyhole wall and scattered regions on the rear wall.

In the following two subsections, we discuss the effects of laser absorption on the shape and fluctuation of both the front and rear keyhole wall.

B. Dynamics of the front keyhole wall

The front keyhole wall is primarily controlled by the fresh ray absorption. The power absorbed of fresh rays is very similar for the three cases, but the front keyhole shape and spatial distribution of fresh ray absorption intensity are quite different in the three cases. In cases 1 and 2, the front keyhole wall is less inclined with noticeable protrusions on the wall. The fresh ray absorption is concentrated on the up side of the protrusions and locally generates very high absorption intensity ($> 3 \times 10^{10}$ W/m^2). In case 3, the front keyhole wall is more inclined and smooth, and the absorption intensity is fairly uniform (2.5×10^{10} W/m^2). The spatial distribution of fresh ray absorption decisively affects the geometry of the front keyhole wall, including the front wall inclination and the protrusion generation on the front wall. The front wall geometry, in turn, alters the distribution of fresh ray absorption.

1. Inclination of front keyhole wall

A series of analytical models has already been proposed to estimate the front wall inclination and keyhole depth based on processing parameters and thermophysical properties of the materials [5,6,43,44]. Inspired by these works, here we present a similar analysis based on our numerical simulation results, which include more information regarding the dynamic thermofluidic phenomena during the laser-induced keyholing process.

The front wall inclination is determined by the combination of the laser scanning speed V_l and the drilling velocity V_d, as estimated by Eq. (1):

$$\tilde{\alpha} = \arctan\left(\frac{V_l}{V_d}\right). \quad (1)$$

Here, V_l is 300, 400, and 800 mm/s for the three cases and V_d can be considered to be the vertical component of the liquid flow velocity on the front keyhole wall. The average V_d is found from the simulations to be 6.5, 3.4, and 2.2 m/s for the three cases. If we plug the V_l and V_d values into Eq. (1), the average inclination angles of the three cases are found to be 3°, 7°, and 20°, reasonably close to the measurement results from the DXR observations and simulations, as already given in Table I.

Note that approximately the same amount of power (130 W) is deposited on the front keyhole wall due to the fresh ray absorption in the three cases, but the resultant V_d is different. The term V_d can be estimated as

$$V_d = \int_{t_{\text{dwell}}} a_d \, dt. \quad (2)$$

Here, a_d is the acceleration for drilling primarily due to the recoil pressure. According to the simulations, the average acceleration due to the recoil pressure is approximately 2.8×10^4, 2.7×10^4, and 2.3×10^4 m/s^2 for the three cases. The term t_{dwell} is the dwell time of fresh rays illuminating the front keyhole wall, which is calculated according to Eq. (3):

$$t_{\text{dwell}} = \frac{d_l}{V_l}. \quad (3)$$

Here, d_l is the diameter of the laser spot, which is 100 μm for our work, and V_l is the laser scanning speed. The fresh ray dwell time is found to be 3.33×10^{-4}, 2.50×10^{-4}, and 1.25×10^{-4} s for the three cases.

In case 1, multiple protrusions on the front wall lead to fresh ray absorption localization on the regions of very small surface area on the up side of those protrusions, and the resulting absorption intensity is rather high (3.2×10^{10} W/m^2). The local temperature becomes very high (around 4200 K) and induces intense evaporation. A strong recoil pressure (as high as 1×10^6 Pa) is available to generate the highest acceleration for drilling (i.e., a_d). Meanwhile, the time for acceleration is the longest (i.e., $t_{\text{dwell}} = 3.33 \times 10^{-4}$ s). The drilling velocity on the front wall is therefore the highest (6.5 m/s).

In case 2, protrusions are also present on the front keyhole wall. In this case, the absorption intensity (3.1×10^{10} W/m^2), surface temperature (4200 K), and recoil pressure (1×10^6 Pa) on the front wall are similar to those in case 1. However, a shorter fresh ray dwell time (2.50×10^{-4} s) is available to accelerate the drilling velocity, leading to a decrease in V_d (3.4 m/s).

In case 3, the front wall is rather flat and the fresh ray absorption is uniformly distributed over the entire front wall, leading to a relatively low absorption intensity (2.5×10^{10} W/m^2) and, hence, the surface temperature is relatively low (around 4000 K). A lower recoil pressure (6×10^5 Pa) is available for an even shorter fresh ray dwell time (1.25×10^{-4} s) to accelerate the drilling velocity. Moreover, since the front keyhole wall is flat, the pressure gradient due to the recoil pressure is along the normal direction of the front wall. Not the entire pressure gradient, but only its vertical component, is used to accelerate the drilling velocity. As a result, the drilling velocity is the lowest (2.2 m/s) in case 3.

2. Protrusion dynamics on the front keyhole wall

Protrusions have been found on the front keyhole wall in cases 1 and 2, and they facilitate the localization of fresh ray absorption to induce high absorption intensity and strong evaporation. The simulations well demonstrate the generation and movement of these protrusions.

For any segment on the front keyhole wall, e.g., the blue segment in Fig. 8(a), if the local inclination angle is α, the incident angle β of the incident fresh ray on this segment can be calculated as $\beta = 90° - \alpha$. The absorption intensity

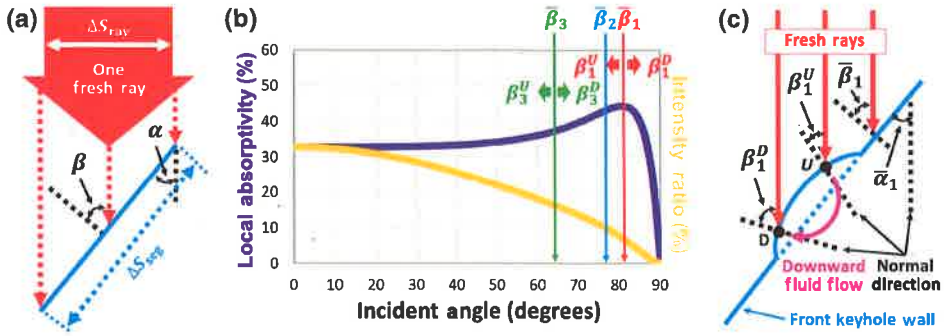

F8:1 FIG. 8. Laser absorption on the keyhole wall. (a) The absorption of one fresh laser ray by a linear segment of the front keyhole wall.
F8:2 (b) Laser absorption by keyhole wall. The purple curve shows the local absorptivity as a function of incident angle. The orange curve
F8:3 shows the ratio of the absorbed laser power intensity on the front keyhole wall over the incident laser power intensity from the fresh
F8:4 laser ray. The red ($\bar{\beta}_1$, β_1^U, β_1^D); blue ($\bar{\beta}_2$); and green ($\bar{\beta}_3$, β_3^U, β_3^D) terms mark out the incident angles of the fresh ray on the front
F8:5 keyhole wall for cases 1, 2, and 3, respectively, and will be used in the discussion of Sec. III B. (c) Nonuniform absorption of fresh
F8:6 rays across a protrusion on the front keyhole wall. Note that the inclination angle and protrusion size are exaggerated in this figure for
F8:7 clarity of illustration.

446 due to the fresh ray can be calculated as

$$447 \quad I_{\text{abs,fresh}} = \frac{I_{\text{fresh}} A(\beta) \Delta S_{\text{ray}}}{\Delta S_{\text{seg}}}$$

$$448 \quad = I_{\text{fresh}} A(\beta) \cos\beta$$

$$449 \quad = I_{\text{fresh}} R_{\text{intensity}}. \qquad (4)$$

450 Here, $I_{\text{abs,fresh}}$ is the absorption intensity on this segment
451 due to the incident fresh ray, the power intensity of which
452 is I_{fresh}. The term $A(\beta)$ is the local laser absorptivity as
453 a function of the incident angle β. The dependence is
454 shown graphically by the purple curve in Fig. 8(b), which
455 is calculated with the Fresnel equation. The term ΔS_{ray} is
456 the cross-section area of the ray. The term ΔS_{seg} is the
457 surface area of the segment, which can be calculated as
458 $\Delta S_{\text{ray}} = \Delta S_{\text{seg}} \cos\beta$. The multiplication term $A(\beta)\cos\beta$
459 calculates the ratio of absorption intensity over incident
460 laser intensity. This intensity ratio, $R_{\text{intensity}}$, as a function
461 of β is shown by the orange curve in Fig. 8(b).

462 In case 1, the protrusions usually start near the top of
463 the front keyhole wall on the convex surface because of
464 the natural transition from the horizontal top surface ahead
465 of the keyhole to the inclined front keyhole wall (see
466 protrusion A in Fig. 9) and these protrusions flow down
467 along the front keyhole wall until they reach the keyhole
468 bottom (see protrusions B and C in Fig. 9). The distribu-
469 tion of fresh ray absorption intensity on these protrusions
470 is not uniform, as illustrated in Fig. 8(c). The average front
471 keyhole wall inclination is $\bar{\alpha}_1 = 9°$ and, correspondingly,
472 the average incident angle of the fresh laser rays on the
473 front wall is $\bar{\beta}_1 = 90° - \bar{\alpha}_1 = 81°$. For any point on the
474 up side of the protrusion (e.g., point U), we can draw
475 the local incident angle of a fresh ray on point U [i.e.,
476 β_1^U in Fig. 8(c)] and find $\beta_1^U < \bar{\beta}_1$. Similarly, if we can
477 find one point from the down side of the protrusion (e.g.,
478 point D) and draw the incident angle of a fresh ray on this
479 point [i.e., β_1^U in Fig. 8(c)], we should find $\beta_1^D > \bar{\beta}_1$. By
480 mapping the values of $\bar{\beta}_1$, β_1^U, and β_1^D in Fig. 8(b), it is
481 evident that the intensity ratio on the up side of the pro-
482 trusion ($R^U_{\text{intensity}}$) is generally higher than that on the down
483 side of the protrusion ($R^D_{\text{intensity}}$), i.e., $R^U_{\text{intensity}} > R^D_{\text{intensity}}$.
484 With similar power intensity I_{fresh} for the fresh rays inci-
485 dent upon points U and D, Eq. (4) gives $I^U_{\text{abs,fresh}} > I^D_{\text{abs,fresh}}$;
486 i.e., the fresh ray absorption intensity is higher on the up
487 side than on the down side of the protrusion. As shown in

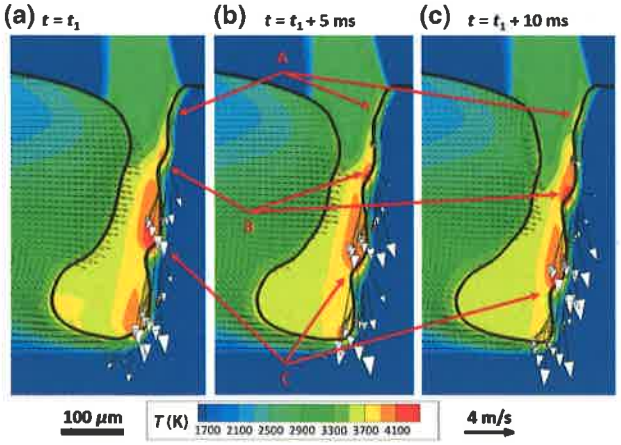

F9:1 FIG. 9. Three consecutive instants in time showing the gener-
F9:2 ation and downward motion of protrusions on the front keyhole
F9:3 wall in case 1. Protrusion A starts to form on the convex sur-
F9:4 face in the transition zone between the horizontal top surface
F9:5 and inclined front keyhole wall. Protrusions B and C are moving
F9:6 downward along the front keyhole wall (notice the high velocity
F9:7 of the fluid flow on the front keyhole wall).

Fig. 6(d), the absorbed intensity is $> 3 \times 10^{10}$ W/m^2 on the up side of the protrusions and $< 2 \times 10^9$ W/m^2 on the down side of the protrusions. In certain scenarios, a portion of the down-side area can even be completely shaded by the protrusion and receive zero illumination by fresh rays. Thanks to the nonuniform distribution of fresh ray absorption, the temperature is considerably higher on the up side than the down side on the protrusion. Figure 5(d) shows the temperature on the up side of the protrusion at around 4200 K, which is well above the boiling point of the metal (3375 K) and causes strong evaporation and recoil pressure (1×10^6 Pa). On the other hand, the temperature on the down side is around 2900 K; hence, no evaporation and recoil pressure are induced. A remarkable pressure difference is created between the two sides of the protrusion, which induces a downward liquid flow, as indicated by the pink arrow in Fig. 8(c). This downward flow causes the protrusions to flow downward along the front keyhole wall as the protrusions grow in size. The intermittent generation of protrusion at the top of the front keyhole wall and their downward motion mean that the front wall appears to be wavy, which is consistent with the DXR observation for case 1.

In case 2, the average front keyhole wall inclination is $\bar{\alpha}_2 = 13°$ and, correspondingly, the average incident angle of the fresh laser rays on the front wall is $\bar{\beta}_2 = 77°$. Protrusions are also found in the DXR observations and in the numerical simulations for this case for reasons identical to those described earlier in case 1. In case 3, the front keyhole wall becomes very flat and no protrusions are observed in the DXR measurements and the simulation. This suggests that the front wall becomes more resistant to protrusion generation compared to cases 1 and 2. The average front keyhole wall inclination for case 3 is $\bar{\alpha}_3 = 26°$ and, correspondingly, the average incident angle of the fresh laser rays on the front wall is $\bar{\beta}_3 = 64°$. Given a random protrusion on the front wall [similar to the one in Fig. 8(c)], the incident angle of fresh rays on the up side and down side of the protrusion (denoted as β_3^U and β_3^D) are slightly different than $\bar{\beta}_3$. As shown in Fig. 8(b), the intensity ratio for both β_3^U and β_3^D are reasonably high, indicating that both the up side and down side of the protrusion receive sufficient intensity to induce evaporation and recoil pressure. In this case, the liquid metal is driven away from both the up side and down side of the protrusion, and the protrusion is suppressed so that the front wall remains flat. The driven liquid flows around the side of the keyhole and enters the molten pool trailing the keyhole, as described in detail in the next subsection.

C. Dynamics of the rear keyhole wall

The rear keyhole wall is found to have quite different shapes in the three cases. The keyhole width in the upper part of the keyhole is relatively small in cases 1 and 2 but fairly large in case 3. The general shape of the rear keyhole wall is found to be independent of the laser absorption on the rear wall. Instead, it is closely related to the fluid dynamics initiated on the front keyhole wall. Furthermore, the general shape of the rear wall significantly alters the distribution of reflected ray absorption, which strongly affects the fluctuation of the rear wall from its average position.

1. Molten pool fluid dynamics and rear keyhole wall shape

The predicted flow patterns in the molten pool trailing the keyhole are shown in Fig. 10. The pattern is most obvious in case 1. Two vortices are evident on the center plane, indicated by A and B in Fig. 10(a). Vortex A is located in the upper part of the molten pool with a counterclockwise flow, which is primarily driven by the thermocapillary force on the top surface of the molten pool. Vortex B is located in the lower part of the molten pool with a clockwise flow direction. This vortex is initiated on the front keyhole wall. Driven by the recoil pressure, the molten metal flows around the keyhole from the left or right sides and the bottom of the keyhole and enters the

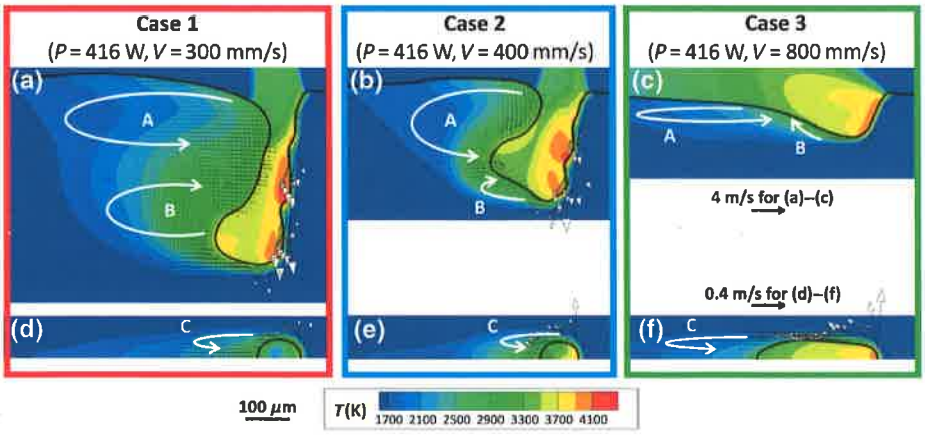

FIG. 10. Simulation results of the temperature and velocity fields in the three selected cases. (a)–(c) Temperature and velocity fields on the center plane from the simulations. (d)–(f) Horizontal planes looking from the top of the keyhole near the surface of the substrate from the simulations. Note that the velocity field for vapor is not shown. The vortices labeled A, B, and C are discussed in Sec. III C 1.

trailing molten pool. This flow moves toward the tail of the molten pool bottom and gradually turns upward along the fusion line. The upward flow collides with the downward flow in the upper vortex, and these two flows both turn to flow toward the rear keyhole wall. In a horizontal plane in the upper part of the molten pool close to the top surface, one vortex can be found in one half of the molten pool, as indicated by C in Fig. 10(d). The flow starts on the front keyhole wall, goes around the keyhole from the side, and moves backward toward the molten pool tail. Then the flow direction reverses to be toward the rear keyhole wall. The flow patterns in cases 2 and 3 are essentially similar to the one in case 1, except that vortex B becomes very small because the molten pool is shallow.

Note that the metal flows in all three vortices, either on the center plane, i.e., vortices A and B in Figs. 10(a)–10(c), or the horizontal plane, i.e., vortex C in Figs. 10(d)–10(f), start with a motion toward the molten pool tail, decelerate, and turn around to flow toward the rear keyhole wall. The liquid pressure near the rear keyhole wall is relatively low (primarily because of the local convex surface and hence the negative surface tension of the rear keyhole wall), so there is usually a pressure gradient toward the rear keyhole wall. The metal flows are accelerated by this pressure gradient as they flow toward the rear keyhole wall. When the metal arrives at the rear keyhole wall, the horizontal component of the flow speed is accelerated to equal V_l. This ensures that the rear keyhole wall can catch up with the front keyhole wall so that the distance between the front and rear keyhole walls (i.e., the keyhole width) remains relatively constant (with some fluctuation around the average width).

In case 1, as protrusions are generated on the front keyhole wall, the recoil pressure primarily drives the molten metal to flow downward so that its downward component (i.e., the drilling velocity, $V_d = 6.5$ m/s) dominates the resultant flow, as shown in Fig. 10(a). In a horizontal plane in the upper part of the molten pool, close to its top surface, as shown in Fig. 10(d), the backward component of the flow velocity V_b is correspondingly very small ($V_b = 300$ mm/s). This slow backward flow is soon reversed and accelerated to $V_l = 300$ mm/s toward the rear keyhole wall. Since V_b and V_l are both small compared to the scan speed, the velocity reversal process can be completed in a very short time and travel distance so that the rear keyhole wall is very close to the front keyhole wall; i.e., the keyhole width is very small in the upper part of the keyhole. In case 2, the flow velocity in the horizontal plane as shown in Fig. 10(e) is similar to that in case 1 and, hence, the keyhole width is also small in the upper part of the keyhole.

In case 3, however, the front keyhole is more inclined and flatter, and the recoil pressure is more uniformly distributed on the front keyhole wall, which pushes the molten metal around the keyhole from the sides. As shown in Fig. 10(f), the backward flow becomes very fast ($V_b = 700$ mm/s), and it takes a relatively long time and travel distance for the flow to reverse its direction and accelerate to the high laser scanning speed of $V_l = 800$ mm/s in this case. By the time the flow reaches the rear keyhole wall, the front keyhole wall has traveled forward for quite a long distance. Hence, the distance between the front and rear keyhole wall, i.e., the keyhole width, becomes rather large in the upper part of the keyhole.

With the keyhole width in cases 1 and 2 being small near the top surface, the "trapping" effect encourages higher absorption for reflected rays (196 W for case 1 and 157 W for case 2). The reflected rays significantly heat the rear keyhole wall (primarily in the lower portion) to above the boiling point. Local evaporation and recoil pressure is induced, pushing the rear keyhole wall backward and enhancing the keyhole width. With the keyhole wall area much larger in case 1 (approximately 7×10^{-8} m^2) than in case 2 (approximately 4.5×10^{-8} m^2), the reflected ray absorption intensity density should be generally lower in case 1 (averaged at approximately 2.8×10^9 W/m^2) than in case 2 (averaged at approximately 3.5×10^9 W/m^2). As a result, the temperature on the rear keyhole wall in case 1 averages approximately 3300 K with the maximum value above 3600 K, while in case 2 the average temperature is above 3400 K with the maximum value above 3700 K. Because of the slightly higher temperature in case 2, a higher recoil pressure is available on the rear wall to push it farther away from the front wall. Therefore, the keyhole width is larger in case 2 (120 μm) than in case 1 (73 μm), as given in Fig. 3.

In case 3, the keyhole width is rather large near the surface of the keyhole, which offers a large exit for the rays to escape. According to our simulation, all the reflected rays will only be absorbed once by the rear keyhole wall, and their reflections will be able to leave the keyhole. Therefore, the reflected ray absorption power is drastically reduced to 56 W and it causes no evaporation on the rear keyhole wall to modify the general shape of the keyhole.

2. Dynamic fluctuation of rear keyhole wall

Strong keyhole fluctuation is found in cases 1 and 2, and it is primarily caused by the random movement of the rear keyhole wall away from its general shape. Such random movement of the rear keyhole wall results from the randomly varying distribution of reflected rays absorbed on the rear keyhole wall, which is initiated by the wavy front from the protrusions on the front keyhole wall. While the fresh rays are presumably parallel to each other before they land on the protrusions, the reflected rays follow different directions and illuminate the rear keyhole wall at different locations. The directions of the reflected rays become essentially random beyond the first reflection. Therefore, no fixed pattern of absorption intensity distribution can be

TABLE II. Order of magnitude of the major forces driving the molten pool flow and keyhole evolution. These forces are evaluated at the front keyhole wall, rear keyhole wall, and top surface of the molten pool in the three selected cases studied in this paper.

	Case 1 $P = 416$ W $V = 300$ mm/s	Case 2 $P = 416$ W $V = 400$ mm/s	Case 3 $P = 416$ W $V = 800$ mm/s
Front keyhole wall			
Maximum temperature (K)	~ 4200	~ 4200	~ 4000
Maximum recoil pressure (Pa)	10^6	10^6	10^5
Maximum curvature (1/m)	-10^4	-10^4	-10^4
Maximum capillary force (Pa)	-10^4	-10^4	-10^4
Maximum temperature gradient (K/s)	10^7	10^7	10^7
Maximum thermocapillary force (Pa)	10^4	10^4	10^4
Rear keyhole wall			
Maximum temperature (K)	~ 3600	~ 3700	~ 2800
Maximum recoil pressure (Pa)	10^5	10^5	0
Maximum curvature (1/m)	-10^4	-10^4	-10^4
Maximum capillary force (Pa)	-10^4	-10^4	-10^4
Maximum temperature gradient (K/s)	10^6	10^6	10^6
Maximum thermocapillary force (Pa)	10^3	10^3	10^3
Top surface of molten pool			
Maximum temperature (K)	< 3000	< 3000	< 3000
Maximum recoil pressure (Pa)	0	0	0
Maximum curvature (1/m)	10^3	10^3	-10^3
Maximum capillary force (Pa)	10^3	10^3	-10^3
Maximum temperature gradient (K/s)	10^6	10^6	10^6
Maximum thermocapillary force (Pa)	10^3	10^3	10^3

found for reflected rays, and hot spots with high absorption intensities can appear at random locations. At each hot spot, local evaporation is induced and recoil pressure is generated that pushes the rear keyhole wall backward, creating a local dent on the rear keyhole wall. As the hot spots wander, the dents move accordingly. There is a hot spot near the bottom in Fig. 5(f) and also around the middle depth in Fig. 5(h).

The fluctuation is significantly reduced in case 3 for two reasons. First, the front keyhole wall is nearly flat, with a relatively uniform distribution of laser absorption and recoil pressure. This helps the molten metal on the front keyhole wall to develop a steady flow going around the keyhole to build a stable rear keyhole wall. Second, the reflected ray absorption is insignificant on the rear keyhole wall. No evaporation is induced and thus no meaningful disturbances on the rear keyhole wall.

D. Effect of major forces on the keyhole dynamics

After the discussion of the laser absorption and the dynamic phenomena on the front and rear keyhole wall, here we present a direct comparison of various driving forces for both the molten pool flow and keyhole evolution. The major driving forces to be investigated are the recoil pressure, capillary force, and thermocapillary force. The orders of magnitude of these forces at different locations of the keyhole are calculated from the simulation results (formula given in Appendix B) and are listed in Table II. Note that the recoil pressure and capillary force are applied along the normal direction of the molten pool surface and keyhole wall, while the thermocapillary force is applied along the tangential direction.

On the front keyhole wall, the temperature is above 4000 K because of the intensive heating from the fresh laser rays, which induces strong evaporation to generate a strong recoil pressure on the order of $10^5 - 10^6$ Pa. This pressure is applied along the normal direction of the keyhole wall toward the liquid region and acts as the major force to maintain the inclined front keyhole wall while pushing it forward. Since the front keyhole wall is a concave interface, the curvature [K in Eq. (B8)] is negative on the order of -10^4 m^{-1}. With the surface tension ~~coefficient~~ [γ in Eq. (B8)] being 1.6 for the liquid metal, the capillary force is on the order of -10^4 Pa. While this force acts along the opposite direction with respect to the recoil pressure, it is at least 2 orders of magnitude smaller and therefore is overruled by the recoil pressure. With the maximum surface temperature gradient [$\nabla_s T$ in Eq. (B3)] on the order of 10^7 K/m and the surface tension coefficient [$\partial\gamma/\partial T$ in Eq. (B3)] being 0.0043 for the liquid metal, the thermocapillary force is on the order of 10^4 Pa. Although this force is also 2 orders of magnitude smaller than the recoil pressure, it acts along a different direction from that of the recoil pressure and hence is not totally overruled. It can

still effectively drive the liquid metal on the interface to flow from hot regions to cold regions (i.e., the Marangoni flow).

On the rear keyhole wall, the temperature is still above the boiling point in cases 1 and 2. The recoil pressure is on the order of 10^5 Pa and is still dominant over the capillary force, which is on the order of -10^4 Pa. However, the temperature of the rear keyhole wall drops below the boiling point in case 3, where no evaporation or recoil pressure is available. The capillary force becomes dominant along the normal direction of the rear keyhole wall. Along the tangential direction, the thermocapillary force is on the order of 10^3 Pa in all three cases and still effectively drives a Marangoni flow on the rear keyhole wall.

On the top surface of the molten pool, the temperature is usually below the boiling point and, hence, no recoil pressure is available. This area is primarily controlled by the capillary force and thermocapillary force, both of which are on the order of magnitude of 10^3 Pa. The capillary force tends to suppress any unevenness on the top surface. The thermocapillary force drives the Marangoni flow toward the tail and the side of the molten pool and is primarily responsible for the development of vortex A in Figs. 10(a)–10(c).

IV. CONCLUSIONS

In this paper, we present a combination of an advanced multiphysics numerical model with state-of-the-art dynamic x-ray radiography experiments to understand the dynamic phenomena of laser-induced keyholing in stainless steel 304. On the experimental side, *in situ* DXR experiments provide observations of the keyhole shape and fluctuation as a function of laser power and scanning speed. As the laser scanning speed is increased at a constant power, the keyhole depth decreases, the front wall inclination and keyhole width increase, and the magnitude of keyhole fluctuation decreases. On the modeling side, our multiphysics model successfully reproduces the typical shapes observed by DXR under different conditions. Moreover, the models provide information regarding the distribution of laser absorption on the keyhole walls and its effects on evaporation, thermofluidic flow, and keyhole shape and fluctuation, all of which are inaccessible via experiment.

On the front keyhole wall, the phenomena are dominated by the absorption of fresh rays. In the case of a lower scanning speed, a higher recoil pressure and a longer fresh ray dwell time are available to accelerate drilling on the front wall, leading to a higher drilling velocity and a smaller inclination angle of the front wall. The incident angle of fresh rays on the front wall is closer to 90°, and the fresh ray absorption becomes less stable. Protrusions form on the top of the front wall and flow downward, causing unstable wavy fluctuation of the front wall. At higher scanning speeds, the front wall is more inclined and the fresh ray absorption becomes more stable, generating a flat and stable front wall.

On the rear keyhole wall, the general shape is primarily determined by the fluid dynamics initiated on the front keyhole wall, and the reflected ray absorption is mainly responsible for the fluctuation of the rear wall from its nominal shape. At lower scanning speeds, the melt flow initiated on the front keyhole wall circulates around the keyhole with a lower speed along the horizontal direction. This slow horizontal flow immediately fills the empty space behind the keyhole, resulting in a smaller keyhole width. The smaller keyhole width significantly enhances multiple reflection of the laser light, resulting in higher absorbed power from reflected ray absorption. The distribution of the reflected ray absorption varies significantly over the rear keyhole wall (especially in the lower portion) and causes the rear keyhole wall to fluctuate. At higher scanning speeds, the melt flow goes around the keyhole at a much higher speed along the horizontal direction. The fast horizontal flow does not immediately fill the empty space behind the keyhole, resulting in a larger keyhole width. The reflected ray absorption is considerably lower and does not cause any noticeable fluctuation of the rear keyhole wall.

Multiple driving forces (namely, recoil pressure, capillary force, and thermocapillary force) exist on the molten pool surface and keyhole wall, and they are of different significance to the molten pool flow and keyhole behavior. Along the normal direction of the interface, the recoil pressure pushes the molten metal away, thus maintaining the opening of the keyhole, while the capillary force tends to suppress any unevenness of the interface. The recoil pressure from evaporation (when present) is usually orders of magnitude larger than the capillary force on both the front and rear keyhole wall, and the capillary force is only significant when the surface temperature is below the boiling point. The thermocapillary force is active along the tangent direction of the interface and drives Marangoni flow. The thermocapillary force is also orders of magnitude smaller than the recoil pressure but its effect is always present.

The combination of DXR observation and multiphysics modeling provides a valuable framework for understanding the complex phenomena in laser-induced keyholes. The framework is expected to contribute to understanding the mechanisms of pore/spatter formation in laser-based additive manufacturing and welding processes.

ACKNOWLEDGMENTS

N.K. and A.D.S. acknowledge the financial support from the Department of Defense Office of Economic Adjustment under Grant No. ST1605-19-03. X.L. and

W.T. thank the financial support from the National Science Foundation under Grant No. CMMI-1752218 and the technical support from the Center for High-Performance Computing at the University of Utah. R.C. and A.D.R. thank the Northrop Grumman Corporation for support of this research. C.Z., N.P., and T.S. are grateful for the Laboratory Directed Research and Development (LDRD) funding from Argonne National Laboratory, provided by the Director, Office of Science, of the U.S. Department of Energy under Contract No. DE-AC02-06CH11357. This research uses resources of the Advanced Photon Source, a U.S. Department of Energy (DOE) Office of Science User Facility operated for the DOE Office of Science by Argonne National Laboratory under Contract No. DE-AC02-06CH11357.

APPENDIX A: METHODOLOGY FOR IN SITU OBSERVATION OF LASER-INDUCED KEYHOLE WITH DYNAMIC X-RAY RADIOGRAPHY

High-speed dynamic x-ray radiography experiments are performed at the 32-ID-B beamline at the APS. Figure 11 shows a schematic of the experimental setup. In each case, a SS304 substrate about 400 μm thick is processed with a specific combination of laser power and scanning speed. The metal specimen is placed inside a SS chamber filled with argon gas to create an inert environment. The experiments are conducted at room temperature without preheating of the metal specimens. A laser beam of approximately 100 μm diameter, shown in Fig. 11, is used to scan along the centerline of the metal plate, orthogonal to the x-ray beam. The high-speed imaging camera captures a side view of the laser keyhole shape that is exposed on the x-ray detectors and records full field x-ray images with a rate of 50 kHz and a spatial resolution of about 2 μm per pixel.

Experiments are performed in the parameter window of interest to metal AM. The laser power P is varied between 208 and 520 W with increments of 104 W and the laser scanning speed V between 300 and 1200 mm/s with increments of 100 or 200 mm/s. For the purpose of this study, 14 combinations of P and V are tested using the DXR experiment to explore typical cases of the keyhole formation.

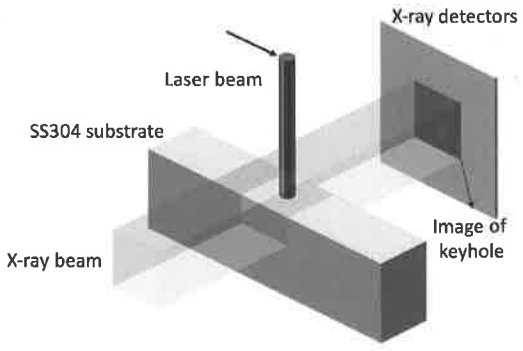

FIG. 11. Sketch of dynamic x-ray radiography experiments. The laser scanning direction is shown by the black arrow.

APPENDIX B: FORMULATION OF THE MULTIPHYSICS MODELING OF LASER-INDUCED KEYHOLE

A multiphysics model is employed to account for keyhole wall movement, laser-matter interaction, and multiphase and multispecies thermofluidic flow in the laser-induced keyhole and molten pool. Model inputs include the laser parameters (laser power, spot size, power distribution, scanning speed); substrate geometry; and material properties. The model then predicts the 3D keyhole shape and the 3D distributions of temperature, pressure, and velocity in solid, liquid, and gas phases. The primary formulations of the model are briefly described in what follows, with a more detailed description of the model provided in Refs. [32] and [33].

In the current model, the level-set (LS) method [45] is used to track the interface between the condensed phases (solid and liquid metal) and noncondensed phases (ambient gas and metallic vapor). The LS equation is written as

$$\frac{\partial \varphi}{\partial t} + \left(\vec{V}_c - \frac{m_{\text{evap}}}{\rho_c}\cdot\vec{N}\right)\cdot\nabla\varphi = 0. \qquad \text{(B1)}$$

In Eq. (B1), φ is the LS function, which quantifies the distance from the centroid of a control volume to the molten pool surface. The molten pool surface (with a portion of it being the keyhole wall) is captured by the zero iso-LS surface, and the LS function is defined to be negative in the condensed phases and positive in the noncondensed phases. The two terms in the bracket of the left-hand side (lhs) of Eq. (B1) are two components that drive the interface motion. The first term, $\vec{V}_c$, is the convection velocity of the condensed phase at the interface. The second term is the surface recession velocity due to evaporation, with m_{evap} as the interface evaporation rate, ρ_c as the density of the condensed phase, and $\vec{N}$ as the unit normal vector at the interface pointing to the noncondensed phases. We adopt the calculation of m_{evap} used by a numerical model [27] that was originally derived in Ref. [46].

The transport phenomena in all phases are governed by the conservation of mass, momentum, energy, and chemical species, which can be written, respectively, as

$$\frac{\partial \rho}{\partial t} + \nabla\cdot(\rho\vec{V}) = 0, \qquad \text{(B2)}$$

$$\frac{\partial \rho \vec{V}}{\partial t} + \nabla \cdot (\rho \vec{V}\vec{V}) = -\nabla p + \nabla \cdot (\mu \nabla \vec{V}) - \frac{\mu}{\kappa}\vec{V} + \rho_r \vec{g}\beta_T (T - T_r) + \nabla_s T \frac{\partial \gamma}{\partial T}\delta_m(\varphi), \quad \text{(B3)}$$

$$\frac{\partial \rho h}{\partial t} + \nabla \cdot (\rho \vec{V} h) = \nabla \cdot (k \nabla T), \quad \text{(B4)}$$

$$\frac{\partial \rho Y}{\partial t} + \nabla \cdot (\rho \vec{V} Y) = \nabla \cdot (\rho D \nabla Y). \quad \text{(B5)}$$

In Eqs. (B2)–(B5), ρ is the density, $\vec{V}$ is the velocity, p is the pressure, μ is the viscosity, κ is the isotropic permeability in the Kozeny-Carman equation, ρ_r is a reference density at the reference temperature T_r, $\vec{g}$ is the gravitational force vector, β_T is the thermal expansion coefficient, T is the temperature, $\nabla_s T$ is the surface gradient of temperature, γ is the surface tension, $\partial\gamma/\partial T$ is the surface tension coefficient, $\delta_m(\varphi)$ is the modified delta function, h is the enthalpy, k is the thermal conductivity, Y is the mass fraction of iron vapor in the ambient gas, and D is the mass diffusivity of iron vapor. Note that the third through fifth terms on the right-hand side (rhs) of Eq. (B3) represent the dragging force in the mushy region, the thermal-buoyancy force, and the thermal-capillary force, respectively.

At the interface between the condensed and noncondensed phases, a set of jump conditions is enforced as boundary conditions of Eqs. (B2)–(B5). We use the notation $\lfloor X \rfloor$ to denote the jump between the condensed and noncondensed phases of a physical quantity X. First, a jump in temperature is enforced according to the theory of the Knudsen layer [47]:

$$\lfloor X \rfloor = T_c - T_{nc}, \quad \text{(B6)}$$

where T_c and T_{nc} are the temperature of the condensed and noncondensed phase at the interface and are calculated according to Ref. [47]. The other jump conditions are obtained from the conservation of mass, momentum, and energy across the interface [48]. The mass conservation is written as

$$\lfloor V_N \rfloor = m_{evap}\left\lfloor \frac{1}{\rho} \right\rfloor, \quad \text{(B7)}$$

where V_N is the velocity normal to the interface. Equation (B7) enforces a jump of the velocity normal across the interface that results from evaporation. The momentum conservation is written as

$$\lfloor p \rfloor = \gamma K + p_{recoil}(T_c), \quad \text{(B8)}$$

where K is the curvature of molten pool surface and p_{recoil} is the recoil pressure generated by the metal vapor. The term p_{recoil} is a function of T_c and is given in Refs. [32] and [33]. Equation (B8) states that the pressure jump on the lhs is balanced by the summation of capillary force and recoil pressure on the rhs. Finally, the energy conservation is written as

$$\lfloor k \nabla T \rfloor = Q_{laser} - \sigma\epsilon(T^4 - T_\infty^4) - m_{evap} L_{evap}, \quad \text{(B9)}$$

where Q_{laser} is the power intensity of laser absorption, σ is the Stefan-Boltzmann constant, ϵ is the emissivity, T_∞ is the ambient temperature, and L_{evap} is the latent heat of evaporation. The lhs of Eq. (B9) represents the jump of the conductive heat flux. The three terms on the rhs are the heat fluxes due to laser absorption, radiation, and evaporation, respectively.

The term Q_{laser} is predicted by a ray-tracing model [32]. The laser is divided into a finite number of rays, each with specific size, position, direction, and power. Upon each incidence of the ray on the keyhole wall, the power of the ray is partially absorbed by the surface according to the local laser absorptivity A, and the remainder of the power goes to the reflected rays, with the reflected direction determined by the law of reflection. The keyhole wall is divided into a finite number of segments in the model, and Q_{laser} for each segment is calculated by dividing the power absorption on each segment by the area of the segment. An example of predicted distribution of Q_{laser} over the entire keyhole is given in Fig. 4(b). Note that A is calculated as a function of the laser incident angle, χ, according to the Fresnel equation

$$A(\chi) = 1 - \frac{1}{2} \times \left[\frac{1 + (1 - \epsilon_c \cos\chi)^2}{1 + (1 + \epsilon_c \cos\chi)^2} + \frac{\epsilon_c^2 - 2\epsilon_c \cos\chi + 2\cos^2\chi}{\epsilon_c^2 + 2\epsilon_c \cos\chi + 2\cos^2\chi}\right]. \quad \text{(B10)}$$

Here, ϵ_c is a material constant related to its electrical conductance. The laser is assumed unpolarized in this work, so the absorptivity is the average of the p-polarized and s-polarized lasers. The calculated absorptivity is shown by the purple curve in Fig. 8(b).

All the governing equations are solved using an in-house numerical solver based on the preconditioning method [49]. All the boundary conditions are treated with a "sharp interface" method [50]. For all the simulations in this work, the laser parameters and substrate geometry are set to be identical to those in the corresponding subset of DXR experiments, and the physical properties of SS304 are obtained from Refs. [32,33]. The three forces of interest in Table II, namely, the recoil pressure, capillary force, and thermocapillary force, are calculated using the terms p_{recoil}, γK, and $\nabla_s T \cdot \partial\gamma/\partial T$, respectively, in Eqs. (B3) and (B8).

[1] A. Matsunawa, J. Kim, N. Seto, M. Mizutani, and S. Katayama, Dynamics of keyhole and molten pool in laser welding, J. Laser Appl. **10**, 247 (1998).

[2] N. P. Calta, J. Wang, A. M. Kiss, A. A. Martin, P. J. Depond, G. M. Guss, V. Thampy, A. Y. Fong, J. Weker, K. H. Stone, C. J. Tassone, M. J. Kramer, M. F. Toney, A. Van Buuren, and M. J. Matthews, An instrument for in situ time-resolved X-ray imaging and diffraction of laser powder bed fusion additive manufacturing processes, Rev. Sci. Instrum. **89**, 055101 (2018).

[3] J. Weberpals and F. Dausinger, in *Int. Congress on Appl. Lasers & Electro-Optics* (LIA, 2008), Vol. 2008, p. 704.

[4] R. Cunningham, C. Zhao, N. Parab, C. Kantzos, J. Pauza, K. Fezzaa, T. Sun, and A. D. Rollett, Keyhole threshold and morphology in laser melting revealed by ultrahigh-speed X-ray imaging, Science **363**, 849 (2019).

[5] R. Fabbro, Melt pool and keyhole behaviour analysis for deep penetration laser welding, J. Phys. D. Appl. Phys. **43**, 445501 (2010).

[6] R. Fabbro, S. Slimani, F. Coste, and F. Briand, Study of keyhole behaviour for full penetration Nd–Yag CW laser welding, J. Phys. D. Appl. Phys. **38**, 1881 (2005).

[7] R. Fabbro, S. Slimani, I. Doudet, F. Coste, and F. Briand, Experimental study of the dynamical coupling between the induced vapour plume and the melt pool for Nd–Yag CW laser welding, J. Phys. D. Appl. Phys. **39**, 394 (2006).

[8] I. Eriksson, J. Powell, and A. F. H. Kaplan, Melt behavior on the keyhole front during high speed laser welding, Opt. Lasers Eng. **51**, 735 (2013).

[9] Y. Zhang, G. Chen, H. Wei, and J. Zhang, A novel "sandwich" method for observation of the keyhole in deep penetration laser welding, Opt. Lasers Eng. **46**, 133 (2008).

[10] S. Li, G. Chen, M. Zhang, Y. Zhou, and Y. Zhang, Dynamic keyhole profile during high-power deep-penetration laser welding, J. Mater. Process Tech. **214**, 565 (2014).

[11] Y. Zhang, Q. Lin, X. Yin, S. Li, and J. Deng, Experimental research on the dynamic behaviors of the keyhole and molten pool in laser deep-penetration welding, J. Phys. D. Appl. Phys. **51**, 145602 (2018).

[12] F. Fetzer, P. Berger, H. Hu, R. Weber, and T. Graf, in *High-Power Laser Mat Process: Applications, Diagnostics, and Systems VII* (2018), Vol. 10525, p. 105250D.

[13] C. Zhao, K. Fezzaa, R. Cunningham, H. Wen, F. Carlo, L. Chen, A. D. Rollett, and T. Sun, Real-time monitoring of laser powder bed fusion process using high-speed X-ray imaging and diffraction, Sci. Rep. **7**, 3602 (2017).

[14] L. I. Escano, N. D. Parab, L. Xiong, Q. Guo, C. Zhao, K. Fezzaa, W. Everhart, T. Sun, and L. Chen, Revealing particle-scale powder spreading dynamics in powder-bed-based additive manufacturing process by high-speed X-ray imaging, Sci. Rep. **8**, 15079 (2018).

[15] N. D. Parab, C. Zhao, R. Cunningham, L. I. Escano, K. Fezzaa, W. Everhart, A. D. Rollett, L. Chen, and T. Sun, Ultrafast X-ray imaging of laser–metal additive manufacturing processes, J. Synchrotron Radiat. **25** (2018).

[16] Q. Guo, C. Zhao, L. I. Escano, Z. Young, L. Xiong, K. Fezzaa, W. Everhart, B. Brown, T. Sun, and L. Chen, Transient dynamics of powder spattering in laser powder bed fusion additive manufacturing process revealed by in-situ high-speed high-energy X-ray imaging, Acta Mater. **151**, 169 (2018).

[17] A. A. Martin, N. P. Calta, J. A. Hammons, S. A. Khairallah, M. H. Nielsen, R. M. Shuttlesworth, N. Sinclair, M. J. Matthews, J. R. Jeffries, T. M. Willey, and J. R. I. Lee, Ultrafast dynamics of laser-metal interactions in additive manufacturing alloys captured by in situ X-ray imaging, Mater. Today Adv. **1**, 100002 (2019).

[18] Y. Kawahito, N. Matsumoto, Y. Abe, and S. Katayama, Relationship of laser absorption to keyhole behavior in high power fiber laser welding of stainless steel and aluminum alloy, J. Mater. Process. Tech. **211**, 1563 (2011).

[19] J. Trapp, A. M. Rubenchik, G. Guss, and M. J. Matthews, In situ absorptivity measurements of metallic powders during laser powder-bed fusion additive manufacturing, Appl. Mater. Today **9**, 341 (2017).

[20] B. J. Simonds, J. W. Sowards, J. Hadler, E. Pfeif, B. Wilthan, J. Tanner, C. Harris, P. A. Williams, and J. Lehman, Dynamic and absolute measurements of laser coupling efficiency during laser spot welds, Procedia CIRP **74**, 632 (2018).

[21] H. Ki, P. S. Mohanty, and J. Mazumder, in *Int. Congress on Appl. Lasers & Electro-Optics* (LIA, 2001), Vol. 2001, p. 933.

[22] J. Cho and S. Na, Implementation of real-time multiple reflection and Fresnel absorption of laser beam in keyhole, J. Phys. D. Appl. Phys. **39**, 5372 (2006).

[23] A. Kar, T. Rockstroh, and J. Mazumder, Two-dimensional model for laser-induced materials damage: Effects of assist gas and multiple reflections inside the cavity, J. Appl. Phys. **71**, 2560 (1992).

[24] J. Milewski and E. Sklar, Modelling and validation of multiple reflections for enhanced laser welding, Model. Simul. Mater. Sci. Eng. **4**, 305 (1996).

[25] P. Solana and G. Negro, A study of the effect of multiple reflections on the shape of the keyhole in the laser processing of materials, J. Phys. D. Appl. Phys. **30**, 3216 (1997).

[26] P. S. Wei and C. Y. Ho, Beam focusing characteristics effect on energy reflection and absorption in a drilling or welding cavity of paraboloid of revolution, Int. J. Heat Mass Transfer **41**, 3299 (1998).

[27] H. Ki, J. Mazumder, and P. S. Mohanty, Modeling of laser keyhole welding: Part i. mathematical modeling, numerical methodology, role of recoil pressure, multiple reflections, and free surface evolution, Metall. Mater. Trans. A **33**, 1817 (2002).

[28] J. Lee, S. H. Ko, D. F. Farson, and C. D. Yoo, Mechanism of keyhole formation and stability in stationary laser welding, J. Phys. D. Appl. Phys. **35**, 1570 (2002).

[29] J. Zhou, H. Tsai, and P. Wang, Transport phenomena and keyhole dynamics during pulsed laser welding, J. Heat Transfer **128**, 680 (2006).

[30] S. Pang, L. Chen, J. Zhou, Y. Yin, and T. Chen, A three-dimensional sharp interface model for self-consistent keyhole and weld pool dynamics in deep penetration laser welding, J. Phys. D. Appl. Phys. **44**, 025301 (2010).

[31] H. Zhao, W. Niu, B. Zhang, Y. Lei, M. Kodama, and T. Ishide, Modelling of keyhole dynamics and porosity formation considering the adaptive keyhole shape and three-phase coupling during deep-penetration laser welding, J. Phys. D. Appl. Phys. **44**, 485302 (2011).

[32] W. Tan, N. S. Bailey, and Y. C. Shin, Investigation of keyhole plume and molten pool based on a three-dimensional dynamic model with sharp interface formulation, J. Phys. D. Appl. Phys. **46**, 055501 (2013).

[33] W. Tan and Y. C. Shin, Analysis of multi-phase interaction and its effects on keyhole dynamics with a multi-physics numerical model, J. Phys. D. Appl. Phys. **47**, 345501 (2014).

[34] M. Courtois, M. Carin, P. Le Masson, S. Gaied, and M. Balabane, A complete model of keyhole and melt pool dynamics to analyze instabilities and collapse during laser welding, J. Laser Appl. **26**, 042001 (2014).

[35] S. A. Khairallah and A. Anderson, Mesoscopic simulation model of selective laser melting of stainless steel powder, J. Mater. Process. Tech. **214**, 2627 (2014).

[36] S. A. Khairallah, A. T. Anderson, A. Rubenchik, and W. E. King, Laser powder-bed fusion additive manufacturing: Physics of complex melt flow and formation mechanisms of pores, spatter, and denudation zones, Acta Mater. **108**, 36 (2016).

[37] Y. Ai, P. Jiang, X. Shao, P. Li, and C. Wang, A three-dimensional numerical simulation model for weld characteristics analysis in fiber laser keyhole welding, Int. J. Heat Mass Transfer **108**, 614 (2017).

[38] C. Panwisawas, B. Perumal, R. M. Ward, N. Turner, R. P. Turner, J. W. Brooks, and H. C. Basoalto, Keyhole formation and thermal fluid flow-induced porosity during laser fusion welding in titanium alloys: Experimental and modelling, Acta Mater. **126**, 251 (2017).

[39] W. Yan, Y. Qian, W. Ge, S. Lin, W. Liu, F. Lin, and G. J. Wagner, Meso-scale modeling of multiple-layer fabrication process in selective electron beam melting: Inter-layer/track voids formation, Mater. Des. **141**, 210 (2018).

[40] D. Farson, K. Hillsley, J. Sames, and R. Young, Frequency–time characteristics of air-borne signals from laser welds, J. Laser Appl. **8**, 33 (1996).

[41] A. Matsunawa, J. Kim, S. Katayama, and V. V. Semak, in *Int. Congress on Applications of Lasers & Electro-Optics* (LIA, 1996), Vol. 1996, p. B58.

[42] S. Ao, Z. Luo, M. Feng, and F. Yan, Simulation and experimental analysis of acoustic signal characteristics in laser welding, Int. J. Adv. Manuf. Tech. **81**, 277 (2015).

[43] R. Fabbro, M. Dal, P. Peyre, F. Coste, M. Schneider, and V. Gunenthiram, Analysis and possible estimation of keyhole depths evolution, using laser operating parameters and material properties, J. Laser Appl. **30**, 032410 (2018).

[44] R. Fabbro, Scaling laws for the laser welding process in keyhole mode, J. Mater. Process. Tech. **264**, 346 (2019).

[45] S. Osher, and R. Fedkiw, *Level Set Methods and Dynamic Implicit Surfaces* (Springer Science & Business Media, 2002). Vol. 44, p. 77.

[46] T. Ytrehus and S. Østmo, Kinetic theory approach to interphase processes, Int. J. Multiphase Flow **22**, 133 (1996).

[47] C. J. Knight, Theoretical modeling of rapid surface vaporization with back pressure, AIAA J. **17**, 519 (1979).

[48] F. Gibou, L. Chen, D. Nguyen, and S. Banerjee, A level set based sharp interface method for the multiphase incompressible navier–stokes equations with phase change, J. Comput. Phys **222**, 536 (2007).

[49] D. Li, and C. L. Merkle, A unified framework for incompressible and compressible fluid flows, J. Hydrodyn. **18**, 111 (2006).

[50] R. P. Fedkiw, T. Aslam, B. Merriman, and S. Osher, A non-oscillatory eulerian approach to interfaces in multimaterial flows (the ghost fluid method), J. Comput. Phys. **152**, 457 (1999).